





Ferromagnetism in ultrathin surface-free $\text{La}_{0.7}\text{Sr}_{0.3}\text{MnO}_3$ layers in electrostatically defined heterostructures

A. Galdi ^{1,2,*}, N. Coppola ², C. Sacco², L. Maritato², P. Bencok³, P. Steadman³, P. Orgiani ^{4,5} and C. Aruta ⁶

¹*Cornell Laboratory for Accelerator Based Sciences and Education, Cornell University, Ithaca, New York 14853, USA*

²*Dipartimento di Ingegneria Industriale, Università degli Studi di Salerno, 84084 Fisciano (SA) Italy*

³*Diamond Light Source, Didcot OX11 0DE, United Kingdom*

⁴*CNR-IOM, TASC Laboratory in Area Science Park, 34139 Trieste, Italy*

⁵*CNR-SPIN, UOS Salerno, 84084 Fisciano, Italy*

⁶*CNR-SPIN, UOS Roma, Area della Ricerca di Tor Vergata, I-00133 Rome, Italy*



(Received 7 February 2021; accepted 29 July 2021; published 23 August 2021)

Electrostatically defined perovskite oxide heterostructures, in which carriers are confined by the modulation of the A-site ion charge, offer new possibilities of tuning the magnetic properties of manganite oxides. We investigate the preferential orientation of ferromagnetic and antiferromagnetic moments in ultrathin $\text{La}_{0.7}\text{Sr}_{0.3}\text{MnO}_3$ layers embedded in antiferromagnetic SrMnO_3 as they undergo a metal-to-insulator transition with decreasing thickness. Our results evince the role of orbital occupation, metallicity, and competition of different magnetic phases, in absence of spurious effects occurring in thin films as a result of symmetry breaking at $\text{La}_{0.7}\text{Sr}_{0.3}\text{MnO}_3$ interfaces and of incorporation of oxygen vacancies.

DOI: [10.1103/PhysRevMaterials.5.084409](https://doi.org/10.1103/PhysRevMaterials.5.084409)

I. INTRODUCTION

Innovative electronic devices and sensors can be engineered by means of transition-metal oxides (TMO) with perovskite structure, exploiting both the bulk functional properties of the materials and new properties that arise at the interface of different compounds or at very small film thicknesses, as a consequence of epitaxial strain, orbital hybridization, and reduced dimensionality effects [1]. Colossal magnetoresistance manganites, such as $\text{La}_{0.7}\text{Sr}_{0.3}\text{MnO}_3$ (LSMO), are of interest for different classes of devices, such as magnetic sensors and tunnel magnetoresistance devices [2,3].

While bulk LSMO is a metallic ferromagnet, it is well known that ultrathin (few nm thick) films undergo a metal-to-insulator transition with decreasing thickness; the layer characterized by suppressed magnetic and metallic properties is called a “dead layer” [4]. The origin of the dead layer has been recently addressed by several works employing state-of-the-art techniques such as scanning transmission electron microscopy coupled with photoemission [5], electron energy-loss spectroscopy [6], and resonant soft-x-ray reflectivity with polarized photons [7]. The progress in thin-film growth techniques has allowed the reduction of the dead-layer thickness down to less than 6–4 unit cells [7,8].

Several studies have revealed the role of oxygen vacancies in determining the dead-layer thickness in ultrathin LSMO films [8,9]. Oxygen vacancies cannot be completely eliminated by enhancing oxidation, since they are introduced in the layer to compensate for electrostatic potential offset at

the film-substrate interface, but they can be greatly reduced by interface engineering at the film-substrate interface [5] and by use of capping layers on the top surface [7]. Not only the dead-layer thickness but also the magnetic properties of thin films, such as the easy axis, are strongly affected by the choice of substrate, as found for LSMO grown on (110) NdGaO_3 (NGO), (100) SrTiO_3 (STO) [10], or (100) $(\text{LaAlO}_3)_{0.3}(\text{Sr}_2\text{AlTaO}_6)_{0.7}$ [11]. The role of octahedral rotations and tilts induced at the film-substrate interface and of modifications of metal-oxygen hybridization has been evinced by structural probes coupled with spectroscopy [7,12]. These results and many other works on heterostructures [13–16] evince the crucial role of the LSMO interface with other TMO.

The thickness induced metal-insulator transition has been previously investigated in ultrathin LSMO layers in $\text{SrMnO}_3/\text{LSMO}/\text{SrMnO}_3$ (SMO/LSMO/SMO) trilayers and attributed to carrier-confinement effects [17]. These trilayers can be considered electrostatically defined heterostructures [18], since the same transition-metal ion (Mn) occupies the perovskite B-site in all layers, while the average A-site ion charge varies going from the SMO to the LSMO layer, thus realizing a “soft confinement” of the carriers as opposed to the case where the film has an interface with a different TMO or with vacuum. Reducing the system dimensionality is a way to tune the properties of TMO [19–21], but the effect of confinement is hard to disentangle from other phenomena occurring at the film interfaces. In SMO/LSMO/SMO trilayers, the bottom SMO layer acts as a buffer between the substrate and the ultrathin LSMO layers, while the top SMO layer acts as a capping layer, thus reducing the possible influence of the film-substrate interface, and of oxygen depletion at the film surface. The absence

*agaldi@unisa.it

of symmetry breaking, thanks to the presence of Mn in all layers, makes them an ideal system to study the effect of thickness and dimensionality on the properties of ultrathin LSMO layers. In similar manganite-based electrostatically defined heterostructures, the magnetic moments are strongly affected by the presence of manganite-manganite interfaces [22–24]; it is shown that not only charge but also magnetic moments can be spatially confined [18,25]. SMO is an antiferromagnetic insulating compound characterized by a Néel transition at about 230 K; therefore the interaction of the antiferromagnetic moments with the ferromagnetism of the ultrathin LSMO layers needs to be investigated [26]. In the following we report a study on the ferromagnetic and antiferromagnetic moments in SMO/LSMO/SMO trilayers as a function of LSMO layer thickness ranging from 4 to 15 unit cells. The study was performed thanks to x-ray circular dichroism (XMCD) and x-ray magnetic linear dichroism (XMLD) measurements at the Mn $L_{2,3}$ edges at temperatures above and below the SMO Néel temperature.

Our results demonstrate the importance of metallicity in determining the magnetic ground state established at the interface between LSMO and different perovskite oxides.

II. EXPERIMENT

SMO/LSMO/SMO trilayers were grown by molecular-beam epitaxy on (110) NGO substrates using the shuttered layer-by-layer deposition technique, as described elsewhere [17,21]. The NGO substrates were prepared by annealing them in a furnace at 1000 °C in oxygen flow. The samples were grown at substrate temperature of 640 °C in O_2 pressure of 1×10^{-6} mbar, and then cooled in the same deposition pressure. The shutter-opening times were determined by growing $LaMnO_3$ and $SrMnO_3$ calibration samples and monitoring reflection high energy electron diffraction (RHEED) intensity oscillations. A LSMO reference sample 60 unit cells thick was typically grown before each trilayer. The SMO/LSMO/SMO trilayers consist of a bottom SMO layer of about 15 unit cells (u.c.), a LSMO layer of variable thickness (n u.c. thick) and a top SMO layer about 10 u.c. thick. In previous work [17], we studied the properties of SMO/LSMO/SMO trilayers with fixed LSMO thickness and variable thickness of SMO top layer; we verified that a thickness of about 10 u.c. is sufficient to protect the LSMO layer from surface effects, possibly due to the incorporation of oxygen vacancies [5].

The samples were characterized by x-ray diffraction (XRD) and reflectivity (XRR) in Bragg-Brentano mode using Cu K-alpha radiation. The reference LSMO samples grown before the trilayers in the same deposition run were also measured by XRD and XRR in order to obtain the LSMO lattice parameter and verify that the number of unit cells grown corresponds to the number of shuttered periods used in deposition. A SMO reference sample was grown in the same deposition run as the $n = 4$ u.c. trilayer. We measured reciprocal space maps (RSMs) around various crystal orientations for selected samples in order to determine the epitaxial relationship of the heterostructures on the substrate.

Resistance versus temperature measurements were performed using a closed-cycle cryostat in the [10, 320] K range,

using the van der Pauw configuration that allows us to determine the trilayer sheet resistance. LSMO reference samples were measured on a hot plate in the [300, 400] K range to measure the resistivity behavior close to the LSMO Curie temperature (360 K).

We performed x-ray magnetic circular dichroism (XMCD) and x-ray magnetic linear dichroism (XMLD) measurements at the I10 beamline of Diamond Light Source, Didcot, United Kingdom. We measured the Mn $L_{2,3}$ absorption edge at temperatures ranging from 20 to 360 K. The x-ray absorption signal was measured in total electron yield (TEY). The XAS signal is normalized by subtracting a linear background value measured before the edge, and then normalizing the edge jump to unity. A magnetic field parallel to the incident beam was provided by a superconducting electromagnet. The spectra were collected with the incident beam either normal to the sample surface (normal incidence, NI) or forming an angle of 30° with the sample surface (grazing incidence, GI). In NI the magnetic field is along the [110] NGO direction, while in GI the magnetic field is applied along the $[1\bar{1}0]$ or [001] direction.

In XMCD measurements, the difference in absorption between left circularly and right circularly polarized photons is measured, which gives information about the average magnetic moment of the investigated ion (Mn in this case) along the beam direction. By changing the configuration from NI to GI, it is possible to measure the magnetic moment in the direction normal and parallel to the film surface. By applying a magnetic field in the beam direction, it is possible to measure the saturated moments, and, by then measuring XMCD in zero field, the remnant moments are measured.

In x-ray linear dichroism (XLD) measurements, the difference in absorption between linear polarized photons is measured. The measurement is performed in GI, with vertical (V) and horizontal (H) polarized photons. In V polarization, the electric field of the radiation is parallel to the film surface, while it is nearly perpendicular in H polarization; for convention we define the XLD as V-H. XLD is sensitive to the uniaxial anisotropy of the density of states, originating both from preferential orbital occupation of the ions and from the orientation of ferromagnetic (F) and antiferromagnetic (AF) moments. The magnetic only contribution, XMLD, is obtained by removing the orbital contribution, given by subtracting the XLD measured above the magnetic ordering temperature from the one measured below [24]. By applying a sufficiently high magnetic field in the direction of the beam, the F moments can be oriented in the beam direction, thus removing the F contribution to XMLD, assuming that there is no exchange coupling between F and AF moments [27].

These techniques allow us to probe the orbital occupation and the magnetic moments (both ferromagnetic and antiferromagnetic) with the sensitivity required to detect the signal from layers a few unit cells thick.

III. RESULTS

A. Structural and transport properties

In Fig. 1 we report the XRR measurements of three of the investigated trilayer (symbols) samples and the best fit of the reflectivity data (lines). The measurements were fit with

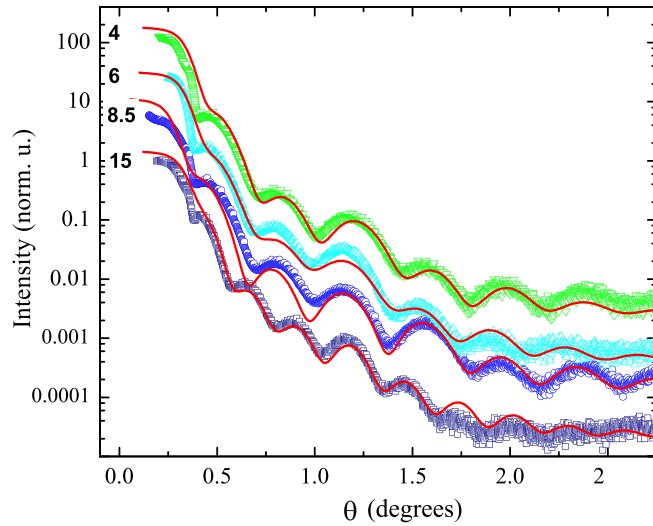


FIG. 1. Symbols: normalized XRR measurements of $n = 15$ (dark blue), $n = 8.5$ (blue), $n = 6$ (cyan) and $n = 4$ (green) trilayers as a function of incidence angle θ . Lines: best fit of the XRR, as described in the text. The curves have been shifted vertically for clarity.

the IMD software [28] by using as fitting parameters the thickness and density of the layers and roughness and diffuseness of the interfaces. To reduce the number of fitting parameters, the top and bottom SMO layers were constrained to have the same density, the ratio of the thickness of the top and bottom was constrained to $2/3$, and the interfaces are constrained to have the same roughness. The thickness of the bottom SMO layer and of the LSMO layers as well as the interface roughness are reported in Table I. The number of LSMO and SMO unit cells is calculated by dividing the thickness $t_{\text{LSMO, SMO}}$ by the measured lattice parameter of LSMO and SMO reference samples grown on (110) NGO substrates. The fitted density of the layers, within the error associated with the fitting parameters, is close to the bulk SMO and LSMO densities (5.5 g/cm^3 and 6.5 g/cm^3 , respectively) [29,30]. Considering the value of the fitted interface roughness σ , reported in Table I, the thickness of the LSMO layer is known within ± 1 u.c. uncertainty, in agreement with our RHEED calibration [17].

In Fig. 2 we report the RSM of the $n = 8.5$ sample around the (332) NGO reflection, corresponding to the (103) reflec-

TABLE I. Fitted thicknesses of the SMO bottom layer and the LSMO layer for the trilayers, σ associated with the interface roughness and lattice parameter of the LSMO control sample grown before the trilayer samples from XRD measurements. The error associated with the parameters is in the last significant digit. A SMO control sample was grown in the same deposition run of the 4 u.c. sample, and the corresponding lattice parameter $c_{\text{SMO}} = 3.79 \text{ \AA}$.

n (u.c.)	t_S (\AA)	t_L (\AA)	σ (\AA)	c_{LSMO} (\AA)
15	57.9	59.2	4.0	3.91
8.5	48.3	34.0	3.0	3.90
6	55.9	23.2	4.0	3.92
4	58.8	16.3	4.5	

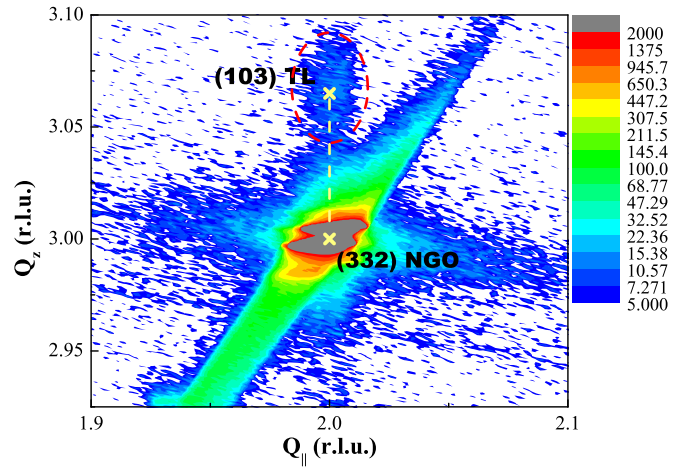


FIG. 2. Reciprocal-space map of the $n = 8.5$ trilayer (TL) sample around the (332) reflection of NGO. The crosses mark the substrate and sample peak positions. The sample peak is circled by the red line.

tion of the (pseudo-)cubic SMO and LSMO unit cells. The map shows that the in-plane lattice parameter of the trilayer sample is matched with the substrate, thus indicating that our samples are fully strained, in agreement to what was found for other SMO/LSMO heterostructures [26].

Resistance versus temperature measurements were performed on the LSMO reference samples grown in the same conditions of the trilayer samples; all the investigated LSMO samples were metallic in the whole temperature range (up to 400 K), in agreement with the phase diagram of LSMO. The SMO reference sample is insulating and its resistance versus temperature curve could not be measured. In Fig. 3 we report the sheet resistance R_s versus temperature measurements of the $n = 4, 6, 8.5$ trilayers. The $n = 8.5, 6$ trilayers are metallic in all the investigated temperature range, while the $n = 4$ trilayer presents a metal-to-insulator transition at about 224 K and an insulator-to-metal transition at about 112 K. A similar behavior has been observed in SMO/LSMO/SMO trilayers grown on STO [17].

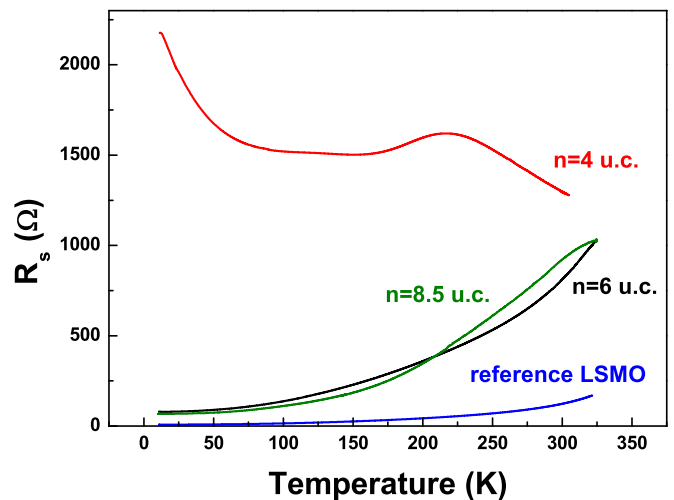


FIG. 3. Sheet resistance of the trilayer samples and of a LSMO reference sample as a function of temperature.

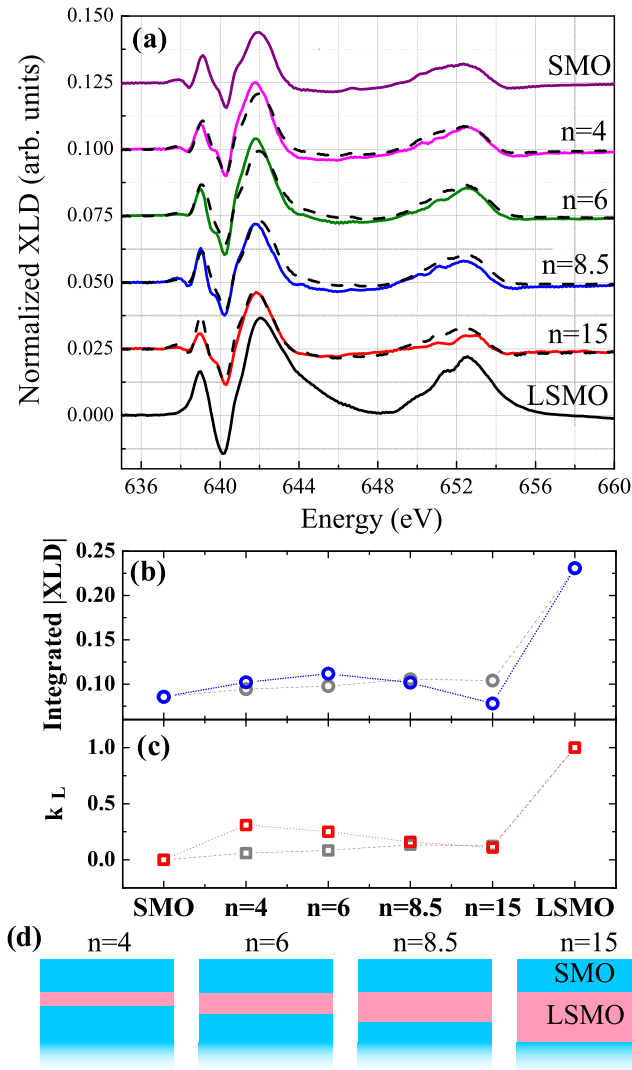


FIG. 4. (a) Continuous lines: normalized XLD spectra of the trilayer samples and of the SMO and LSMO reference samples measured at $T = 250$ K with an applied magnetic field of $2T$, representing the purely orbital component. Dashed lines: composition of the LSMO and SMO spectra that better represents the experimental data. (b) Blue symbols: integral of the absolute value of the XLD spectra. Gray symbols: calculated maximum value of the integral, using the model described in the text. (c) Red symbols: coefficient of the LSMO component of the superposition of spectra in panel (a). Gray symbols: calculated coefficients using the model described in the text. (d) Fraction of the TL samples probed by the TEY measurements.

B. Linear dichroism measurements

In Fig. 4(a) we report the XLD measured at 250 K with an applied magnetic field $\mu_0 H = 2T$ along the $[001]/[1\bar{1}0]$ direction (sufficient to saturate the F moments in the beam direction) for the series of trilayer samples and the LSMO and SMO reference samples; the signal is normalized to the sum of the (V + H) spectrum. These spectra provide the purely orbital XLD, since the temperature is well above the Néel transition of SMO [26] and the F moments are saturated in the direction perpendicular to the light polarization. The LSMO

reference spectrum is typical of compressively strained films, where the preferential $3d e_g$ orbital occupation of Mn ions is $3z^2 - r^2$ [27]. Indeed the LSMO is compressively strained on the NGO substrate, as confirmed by the expanded out-of-plane lattice parameter reported in Table I [the bulk LSMO lattice parameter is 3.89 Å, while the pseudocubic lattice parameter of NGO (110) is 3.86 Å [31]]. The SMO reference XLD is due to Mn with purely $4+$ valence; the two unoccupied Mn e_g orbitals (in-plane $x^2 - y^2$ and out-of-plane $3z^2 - r^2$) are split in energy because of the tensile strain experienced by SMO on NGO (the cubic SMO lattice parameter is 3.804 Å [32]). Consequently the XLD, being the difference between in-plane and out-of-plane absorption signals, exhibits a positive-negative pattern since the $x^2 - y^2$ orbital is at lower energy than the $3z^2 - r^2$ orbital.

The orbital XLD of the trilayer samples can be reproduced by the superposition of the LSMO and SMO XLD spectra $\mu_L^{L,S}$ with coefficients k_S , k_L :

$$\mu_L^{TL}(n) = k_S(n)\mu_L^S + k_L(n)\mu_L^L, \quad (1)$$

as shown by the dashed line curves in Fig. 4(a); the error associated with the coefficients is about 10%. The TEY signal is determined by the thickness of the SMO and LSMO layers and by the exponential attenuation of the secondary electrons generated by the absorption process [33]. Assuming that the XLD of the SMO and LSMO layers is unchanged by the carrier confinement and by the presence of the interfaces, the XLD signal of the trilayers can be calculated by

$$\begin{aligned} \mu_L^{TL}(n) \approx & \mu_L^S(1 - e^{-\frac{2t_S}{3d}}) + \mu_L^L e^{-\frac{2t_S}{3d}}(1 - e^{-\frac{t_L}{d}}) \\ & + \mu_L^S e^{-\frac{2(3t_S+t_L)}{d}}, \end{aligned} \quad (2)$$

where t_S and t_L are the thickness of the SMO bottom and of the LSMO layer, respectively, as obtained by the XRR fit. We use the same attenuation length $d \approx 3$ nm for the SMO and LSMO layers [34], and we neglect the finite thickness of the SMO bottom layer. We find that our data cannot be described by Eq. (2), and even varying the attenuation length or assuming different attenuation lengths in SMO and LSMO does not improve the agreement. In Fig. 4(b) we plot the total XLD signal intensity, obtained as the integral of $|\mu_L|$. The XLD intensity is nonmonotonic and has a maximum for $n = 6$, and it is minimum for $n = 15$. For comparison we report the calculated value of

$$\tilde{k}_S(n) \int_{L_{2,3}} |\mu_L^S| dE + \tilde{k}_L(n) \int_{L_{2,3}} |\mu_L^L| dE \quad (3)$$

using Eq. (2) to obtain coefficients \tilde{k}_L and \tilde{k}_S ; this quantity must be greater or equal to the integral of $|\mu_L^{TL}(n)|$. Instead, the measured XLD intensity exceeds the calculated value, represented by the gray symbols in Fig. 4(b) for $n = 4, 6$, thus indicating an enhancement of the XLD signal for the trilayers characterized by the thinner LSMO layers. Furthermore, the calculated \tilde{k}_L coefficient can be compared with k_L obtained by the fit of Eq. (1) to the experimental data, as shown in Fig. 4(c). For $n < 8.5$, $k_L > \tilde{k}_L$ thus suggesting that it is the XLD signal coming from the LSMO layer that is enhanced for the smaller n trilayers.

In Fig. 5(a) we report the XMLD spectra of all samples except SMO measured with zero applied magnetic field at 20 K,

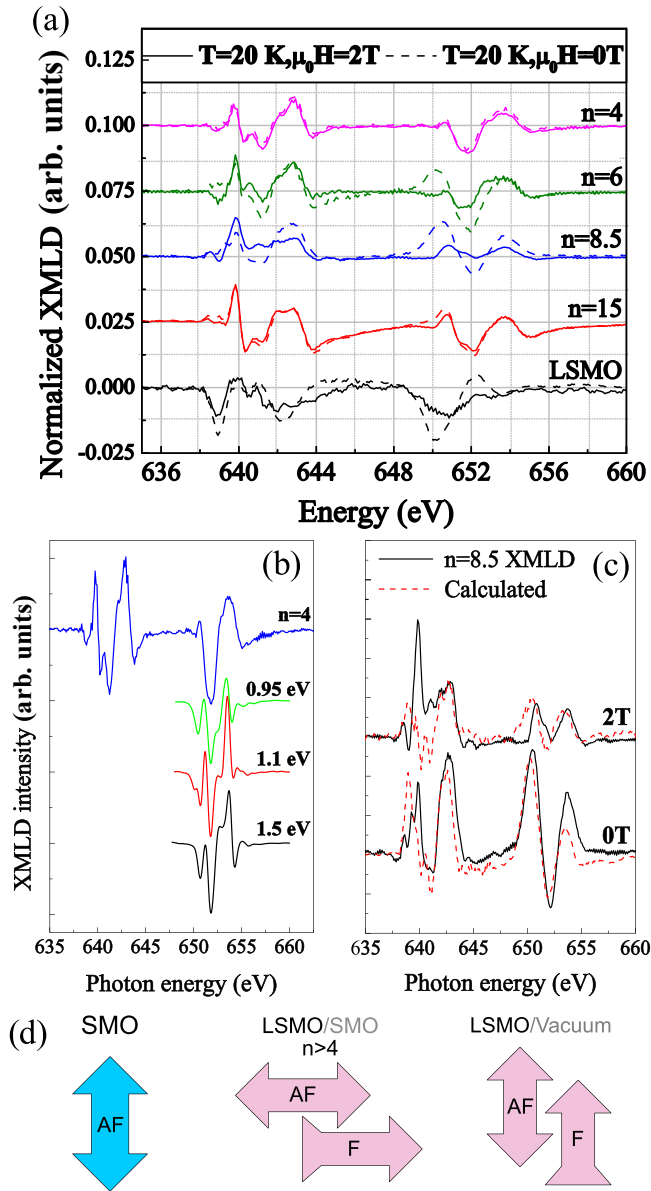


FIG. 5. (a) XMLD spectra of the $n = 4, 6, 8.5$ and 15 TL samples and LSMO reference sample. Dashed lines represent the XMCD in zero applied magnetic field, while solid lines represent the XMCD with F moments saturated in the beam direction. (b) Comparison of the XMLD of the $n = 4$ sample with XMLD atomic simulations for different values of the $10Dq$ parameter. (c) Comparison of the $n = 8.5$ trilayer XMLD with a superposition of the $n = 4$ and of the LSMO spectrum. (d) Orientation of the F and AF magnetic moments as deduced from the XMLD spectra in SMO, LSMO ultrathin layers embedded in SMO and LSMO with vacuum interface. The orientation of the magnetic moments of LSMO embedded in SMO can only be deduced for $n > 4$.

originating from the preferential orientation of both F and AF magnetic moments (dashed lines), and with $\mu_0H = 2T$, originating from AF moments only (full lines). The XMLD of the LSMO sample is characteristic of preferential out-of-plane orientation of the magnetic moments [35]; since the signal is not reversed by the application of magnetic field, both F and AF moments are out of plane. The XMLD of the $n = 4$

sample does not vary with the application of the magnetic field, indicating that the magnetic anisotropy is dominated by the AF moments. Since the LSMO layer is very thin for the $n = 4$ sample, we assume that the XMLD is dominated by a Mn^{4+} contribution, despite not being able to compare with the XMLD of the SMO sample due to its insulating state. To identify the orientation of the AF moments in SMO, in Fig. 5(b) the XMLD of the $n = 4$ sample at L_2 is compared with atomic simulations of Mn^{4+} XMLD performed with the Cowan code using 60% reduced Slater integral, crystal-field splitting $10Dq = 0.95, 1.1, 1.5$ eV, octahedral field tensile distortion parameters $Ds = 4Dt = -0.5$ eV, and magnetic exchange energy of 10 meV with the spin oriented in the out-of-plane direction [36]. Besides some parameter-dependent details, the simulations reproduce the sign of the experimental XMLD, indicating preferential orientation of the magnetic moments in the out-of-plane directions for the SMO layer. If the moments were aligned in-plane, we would have expected the sign of the XMLD to be reversed [23,27]. For the $n = 6, 8.5, 15$ trilayers, the XMLD changes significantly with the application of $\mu_0H = 2T$, thus revealing the presence of an F component. We attribute the F contribution to Mn^{3+} in the LSMO layer, which is known to dominate the XMLD of mixed-valence manganites [27]. The AF XMLD of the $n = 6$ sample is mainly similar to the $n = 4$ spectral shape, while the one of the $n = 8.5, 15$ samples develops different features, intrinsically stronger in the $n = 8.5$ sample.

In Fig. 5(c) the XMLD of the $n = 8.5$ sample is reproduced by a combination of the XMLD spectrum of the $n = 4$ and LSMO samples:

$$\mu_{LM}^{TL}(8.5, H) = A(H)\mu_{LM}^{TL}(4, H) - B(H)\mu_{LM}^L(H), \quad (4)$$

where $\mu_{LM}^{TL}(4, H)$, $\mu_{LM}^L(H)$ are the XMLD of the $n = 4$ and LSMO samples for $\mu_0H = 0, 2$ T. The values of the coefficients that better reproduce the experimental data are $A = 0.4$ for both $\mu_0H = 0, 2$ T (as expected, as the AF contribution from SMO does not change with H), $B(0 \text{ T}) = 0.6$, and $B(2 \text{ T}) = 0.45$. The minus sign before $B(H)$ indicates that the LSMO component in $n = 8.5$ has perpendicular anisotropy with respect to the one of the LSMO reference, i.e., in the sample plane. These coefficients do not correspond to those either fitted or calculated for the XLD case ($k_S = 0.85, k_L = 0.15$). Some features, such as the sharp peak at 640 eV, cannot be reproduced and may be due to different magnetic states arising at the SMO-LSMO interface. In conclusion, the XMLD analysis indicates that, for metallic LSMO embedded in the trilayer heterostructure, the preferential orientation of both F and AF moments is in-plane, as depicted in Fig. 5(d). For the LSMO reference sample, the analysis of XMCD indicates that the XMLD signal is dominated by the contribution of the film-vacuum interface, as discussed in the following.

C. Magnetic circular-dichroism measurements

XMCD measurements were performed at an applied field of $\mu_0H = 2T$ for the $n = 6, 8.5, 15$, and LSMO samples, and at $\mu_0H = 5T$ for the $n = 4$, in order to fully saturate the magnetic moments, and at $0T$ to measure the remnant XMCD. The spectra, collected at GI (along $[001]/[1\bar{1}0]$) and

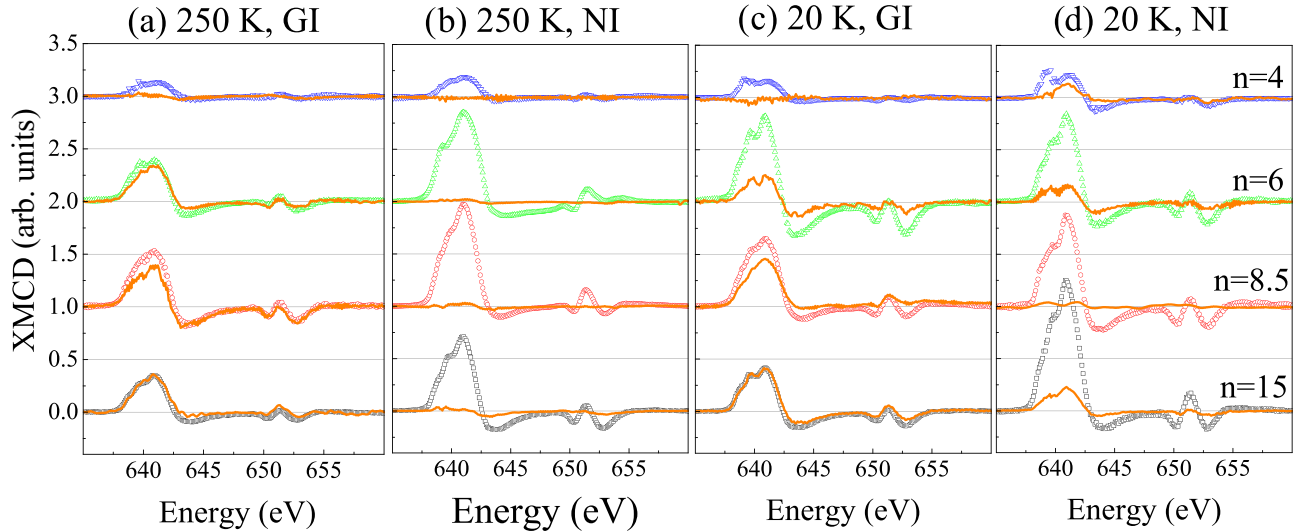


FIG. 6. XMCD spectra measured at (a) 250 K in GI, (b) 250 K in NI, (c) 20 K in GI, (d) 20 K in NI. The spectra are vertically shifted for clarity. Symbols (black for $n = 15$, red for $n = 8.5$, green for $n = 6$, blue for $n = 4$) represent the measurement with the moment saturated by $\mu_0 H = 2T$ ($\mu_0 H = 5T$ for $n = 4$), lines represent the measurements collected in zero field.

NI above (along [110]) (250 K) and below (20 K) the SMO Néel temperature, are reported in Fig. 6. All the samples shows a stronger XMCD signal in the saturated case for NI measurements, although for the $n = 4$ sample the intensity difference between saturated GI and NI measurement is very little. On the other hand the saturated XMCD signal of the reference LSMO sample (not shown) is isotropic within the measurements accuracy. This behavior is observed both at 250 and 20 K. For the trilayer samples at 250 K, we are not able to detect any XMCD signal originating from remnant moments in NI, while the remnant XMCD is quite close to the saturated one in GI for $n > 4$. The $n = 4$ sample does not have any remnant XMCD at high temperature. At 20 K, the remnant signal is detected also in NI. The $n = 4$ sample, in particular, shows remnant XMCD only in NI.

To obtain quantitative information about the ferromagnetic moments, we resort to XMCD sum rules, which allow one to obtain the effective spin moment $m = \langle S_z \rangle + 7/2 \langle T_z \rangle$, where $\langle S_z \rangle$ and $\langle T_z \rangle$ are the expectation values of the projection along the quantization axis of the spin and magnetic-dipole operators, respectively [37]. According to the spin sum rule, the effective spin moment can be obtained by

$$m = \frac{3 \int_{L_3} \mu_M dE - 2 \int_{L_2+L_3} \mu_M dE}{\int_{L_2+L_3} (\mu_{\text{ISO}} - bgn) dE} \frac{3}{2} \langle N_h \rangle, \quad (5)$$

where μ_M is the XMCD spectrum, μ_{ISO} is the isotropic absorption spectrum that can be obtained by averaging the left- and right-polarization spectra, bgn is a continuum background, typically approximated with a 2 : 1 double step-function [38], and $\langle N_h \rangle$ is the number of valence holes. The application of Eq. (5) to the trilayer system is complicated by the heterogeneity of the samples (only a fraction of the sample is ferromagnetic and $\langle N_h \rangle$ varies across the sample thickness). Furthermore, errors in the pre-edge subtraction and normalization of the spectra strongly affect the integral of μ_{ISO} , while μ_M spectra are more robust in this regard. For this

reason we only calculate the ratio of the magnetic moments measured in 0 and 2 T applied magnetic field, $m_{\text{RMN}}/m_{\text{sat}}$, at fixed incidence, so that the dependence on $\langle N_h \rangle$ and on the integral of μ_{ISO} cancels out. The $m_{\text{RMN}}/m_{\text{sat}}$ results are reported in Fig. 7 for the $n = 4, 6, 8.5, 15$ samples and for the LSMO reference sample (60 u.c. thick). For the LSMO sample, we observe that, when the sample is magnetized in-plane (GI measurements), about 80% of the magnetic moment stays aligned when the field $\mu_0 H = 0$, while the remnant signal in NI is only about 10%, indicating that the ferromagnetic easy axis is in the sample plane, and this behavior is quantitatively unchanged by temperature. The magnetic anisotropy is enhanced respect to LSMO in the $n > 4$ trilayer samples at 250 K, for which, within the experimental error, $m_{\text{RMN}}/m_{\text{sat}} = 0$ in the NI measurements, while in GI it is close to the LSMO value. At 20 K we observe a reduction of the magnetic anisotropy: the NI measurements acquire nonzero remnant magnetization, while the GI $m_{\text{RMN}}/m_{\text{sat}}$ is smaller than the 250 K value. In particular, the 20 K $m_{\text{RMN}}/m_{\text{sat}}$ values in GI are smaller for smaller n . For the $n = 8.5$ sample, the NI moments at 0 T could not be evaluated because of problems with the background of the spectra. The $n = 4$ sample has a different behavior: at 250 K $m_{\text{RMN}}/m_{\text{sat}} = 0$ both in GI and NI, while at 20 K $m_{\text{RMN}}/m_{\text{sat}} \approx 0.6$ in NI only.

IV. DISCUSSION

SMO and LSMO are both magnetic oxides whose properties are strongly affected by the ordering, filling, and bandwidth of Mn 3d orbitals [3]. In trilayer samples those properties are modified by the epitaxial strain induced by the NGO substrate, by the presence of sharp LSMO-SMO interfaces and by the reduced thickness of the LSMO layer.

RSM measurements show that the trilayer samples are fully strained on the NGO substrate. Consequently, SMO experiences tensile strain ($\approx -1.5\%$), resulting in the XLD reported in Fig. 4. First-principles calculations indicate that, up to a

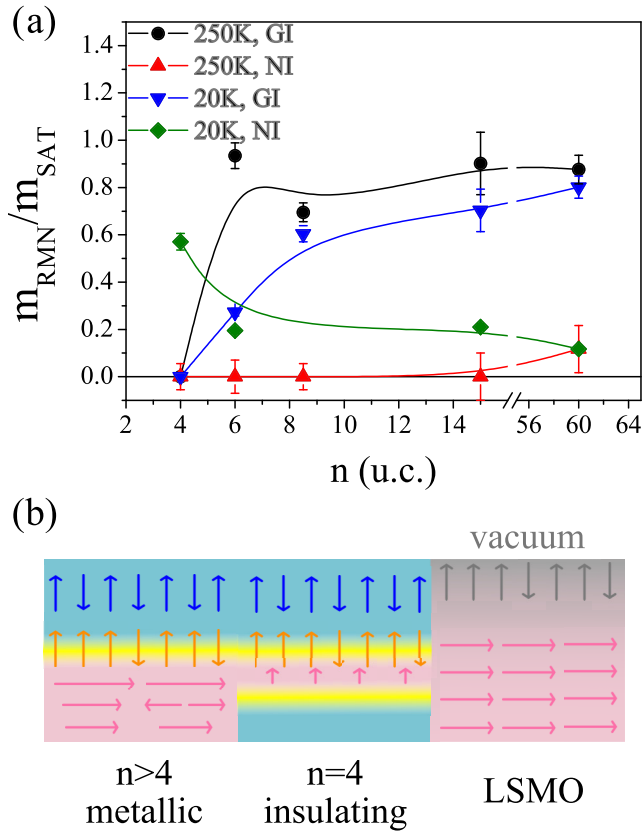


FIG. 7. (a) Ratio between the effective spin moment calculated from the XMCD spectra measured in zero field m_{RMNI} and with $\mu_0 H = 2T, 5T$ m_{sat} . Black circles represent the measurements at 250 K in GI, red triangles at 250 K in NI, blue triangles at 20 K in GI and green diamonds at 20 K in NI. The LSMO sample data are reported for $n = 60$. Lines are guides to the eye. (b) Schematic representing the magnetic easy axes in SMO (AF, blue arrows), LSMO (F and AF, pink arrows), the glassy SMO-LSMO interfaces (orange arrows) and the LSMO-vacuum interface (F and AF, gray arrows).

critical strain of -1.6% , the magnetic ground state is G-type AF [26], and the comparison of XMLD measurements with atomic multiplet calculations in Fig. 5(a) indicates that the AF easy axis is out-of-plane.

LSMO is compressively strained on NGO ($\approx 0.8\%$). It is well assessed that the film-substrate interaction results in uniaxial magnetic anisotropy with the F easy axis along the in-plane $[1\bar{1}0]$ substrate direction [11]. This is confirmed by the XMCD measurements on the LSMO reference sample (see Fig. 7). However, when looking at the XMLD measurements reported in Fig. 4(b), the reference LSMO spectrum is characteristic of Mn^{3+} F and AF moments with out-of-plane orientation [35]. We attribute this signal to the sample surface, which has typically suppressed metallic and magnetic properties due to the incorporation of oxygen vacancies [7]. The symmetry breaking at the sample surface [39] promotes the preferential occupation of out-of-plane Mn $3d$ $3z^2 - r^2$ orbital; consequently, even in highly tensile strained LSMO thin films on SrTiO_3 , an AF phase originating at the sample surface is characterized by out-of-plane aligned AF magnetic moments, i.e., in agreement with the surface preferential or-

bitual occupation [35]. It is reasonable to assume that the magnetic contribution to XLD, originating from the distortion of the density of states induced by the spin-orbit coupling in Mn $3d$ orbitals, is stronger for the more localized electrons in the surface region with suppressed metallic properties, so that the XMLD signal is dominated by surface F and AF moments that orient preferentially in the out-of-plane direction dictated by the orbital ordering. On the other hand, XMCD measurements, which are directly sensitive to the magnetic moments, are dominated by the bulk of the LSMO film, with the expected F in-plane easy axis.

The $R(T)$ curves of the trilayer samples with different n do not show any qualitative difference besides the insulator-to-metal transition for $n = 4$ (Fig. 3). Nevertheless, the XLD measurements of Fig. 4 indicate an enhanced orbital polarization in the thinner LSMO layers, with preferential occupation of the $3d$ $3z^2 - r^2$ orbital (as expected from the sign of the epitaxial strain). This effect is not a consequence of the interface but rather of reduced thickness, since the topmost LSMO-SMO interface is at about the same depth from the surface for all n (same degree of attenuation from the top SMO layer), while we see the effect vanishing altogether with thickness $n \gtrsim 8.5$.

The XMLD data of Fig. 5 show that the F and AF moments in the ultrathin LSMO layers are preferentially oriented in the sample plane for $n > 4$. Most of the XMLD spectrum of the TL samples can be reproduced by a superposition of the $n = 4$ spectrum, that we use as a reference for the SMO AF signal, and of the LSMO with inverted sign. However, the coefficients we use are different from k_L, k_S obtained by the fits of the XLD using Eq. (1), in particular the SMO weight $A < k_S$. This strongly suggests that the observed behavior of the magnetic moments at 20 K is determined by the effects of competition of magnetic orders at the interface. For the nonmetallic $n = 4$ sample, XMLD cannot give information about the very thin LSMO layer; however, XMCD measurements at 20 K reveal that remnant magnetization is only detected in NI (see Figs. 6 and 7), indicating a switch of the F easy axis from in-plane to out-of-plane accompanying the thickness-induced metal-to-insulator transition. Unfortunately, no indication could be obtained about the orientation of the LSMO AF moments for $n = 4$.

We interpret these findings as an enhanced tendency of aligning the (F and AF) magnetic moments in-plane due to the trilayer structure when the LSMO is in the metallic phase. On the other hand, for the nonmetallic $n = 4$ sample, the preferential orientation of the magnetic moments aligns with the preferential out-of-plane orbital occupation of Mn^{3+} ions induced by the substrate strain and enhanced by the reduced dimensionality [21].

This is in agreement with previous observations of $(\text{LaMnO}_3)_{2m}(\text{SrMnO}_3)_m$ digital superlattices. Only for the $m = 1$ sample, characterized by homogeneous electron density and delocalization [40], do both F and AF moments preferentially lie parallel to the interfaces in the sample plane, while for larger m the orientation of the AF moments is determined by the orbital occupation in the insulating LaMnO_3 blocks [23].

The XMCD measurements of Fig. 6 and the ratio between remnant and saturated effective spin moments, $m_{\text{RMNI}}/m_{\text{sat}}$, at

250 K confirm the enhancement of in-plane vs out-of-plane F anisotropy induced by the electrostatically defined interfaces, since in contrast with the LSMO reference sample, no NI m_{RMN} is detected in the trilayer samples.

At 20 K, well below the SMO Néel temperature, the samples acquire remnant magnetization in NI and the GI $m_{\text{RMN}}/m_{\text{sat}}$ is reduced with respect to the 250 K value. We attribute this behavior to the ordering of a new magnetic phase arising from the competition of ferromagnetism and antiferromagnetism at the SMO-LSMO interface. In Ref. [26], the occurrence of exchange bias (at $T < 150$ K) in SMO/LSMO bilayers is attributed to a spin-glass phase occurring at the interface. Our findings suggest that such a state is characterized by preferential out-of-plane orientation of the F moments. The fact that the SMO weight in XMLD at 20 K A is lower than the SMO weight in XLD at 250 K k_s indicates that the glassy F phase extends in the SMO layer. Our experiments are not suitable for the observation of exchange bias, since the samples were cooled in zero magnetic field. However, no enhancement of the coercive field at low temperature (typically observed in exchange-bias systems) is observed in hysteresis cycles measured by XMCD (not reported), leading us to exclude the possibility of establishing exchange bias, probably because of the small LSMO thickness [26]. The interaction between the antiferromagnetism in SMO and the ultrathin LSMO layer may play a role in the stabilization of out-of-plane ferromagnetism in the insulating $n = 4$ sample [41,42].

V. CONCLUSIONS

Electrostatically defined heterostructures allow us to explore the behavior of ultrathin ferromagnetic LSMO layers

at reduced thickness, without being affected by spurious phenomena such as symmetry breaking, orbital hybridization, and the incorporation of oxygen vacancies.

For example, we observe an enhancement of the occupation of the $3z^2 - r^2$ orbital induced by the reduced thickness of the LSMO layer and by the carrier confinement [17], even in samples that are characterized by metallic transport properties.

The behavior of the magnetic moments is strongly affected by the SMO-LSMO interface. Our results show that the preferential orientation of the magnetic moments depends on the metallicity of the LSMO layers, confirming once again its importance in determining the behavior of LSMO-based heterostructures [14,15].

In metallic LSMO ultrathin layers ($n > 4$) the magnetic moments of coexisting AF and F phases are preferentially oriented along the interfaces, regardless of the orbital occupation, while for insulating LSMO layers ($n \leq 4$), the ferromagnetic moments align in the direction of the preferentially occupied Mn $3d e_g$ orbital. The highly anisotropic in-plane magnetic phases are most probably located in the near-interface region [24], as suggested by the small Mn^{3+} contribution to XMLD for the $n = 15$ sample, where the bottom LSMO-SMO interface is deeply buried in the sample.

Ultrathin LSMO layers embedded in SMO offer new possibilities of tailoring the magnetic properties of LSMO without degrading its metallic properties and using a very small band gap material (SMO gap is 0.3 eV), thus preserving electric conductivity [43]. For example, above the SMO Néel temperature, the NI remnant magnetization is fully suppressed, allowing one to linearize the magnetic response in the out-of-plane direction, as required for application in magnetic sensors [11,44].

-
- [1] P. Zubko, S. Gariglio, M. Gabay, P. Ghosez, and J.-M. Triscone, *Annu. Rev. Condens. Matter Phys.* **2**, 141 (2011).
 - [2] T. Venkatesan, M. Rajeswari, Z.-W. Dong, S. B. Ogale, and R. Ramesh, *Philos. Trans. R. Soc. London, Ser. A* **356**, 1661 (1998).
 - [3] D. Pesquera, A. Barla, M. Wojcik, E. Jedryka, F. Bondino, E. Magnano, S. Nappini, D. Gutiérrez, G. Radaelli, G. Herranz, F. Sánchez, and J. Fontcuberta, *Phys. Rev. Appl.* **6**, 034004 (2016).
 - [4] J. Z. Sun, D. W. Abraham, R. A. Rao, and C. B. Eom, *Appl. Phys. Lett.* **74**, 3017 (1999).
 - [5] R. Peng, H. C. Xu, M. Xia, J. F. Zhao, X. Xie, D. F. Xu, B. P. Xie, and D. L. Feng, *Appl. Phys. Lett.* **104**, 081606 (2014).
 - [6] Y. Feng, K. Jin, L. Gu, X. He, C. Ge, Q. Zhang, M. He, Q. Guo, Q. Wan, M. He, H. Lu, and G. Yang, *Sci. Rep.* **6**, 22382 (2016).
 - [7] Z. Liao, N. Gauquelin, R. J. Green, S. Macke, J. Gonnissen, S. Thomas, Z. Zhong, L. Li, L. Si, S. Van Aert *et al.*, *Adv. Funct. Mater.* **27**, 1606717 (2017).
 - [8] L. Fitting Kourkoutis, J. H. Song, H. Y. Hwang, and D. A. Muller, *Proc. Natl. Acad. Sci. USA* **107**, 11682 (2010).
 - [9] C. Wang, K. Jin, L. Gu, H. Lu, S. Li, W. Zhou, R. Zhao, H. Guo, M. He, and G. Yang, *Appl. Phys. Lett.* **102**, 252401 (2013).
 - [10] P. Ghising, B. Samantaray, and Z. Hossain, *Phys. Rev. B* **101**, 024408 (2020).
 - [11] S. K. Chaluvadi, F. Ajejas, P. Orgiani, S. Lebargy, A. Minj, S. Flament, J. Camarero, P. Perna, and L. Mechin, *J. Phys. D: Appl. Phys.* **53**, 375005 (2020).
 - [12] E. J. Moon, P. V. Balachandran, B. J. Kirby, D. J. Keavney, R. J. Sichel-Tissot, C. M. Schlepütz, E. Karapetrova, X. M. Cheng, J. M. Rondinelli, and S. J. May, *Nano Lett.* **14**, 2509 (2014).
 - [13] J. Chakhalian, J. Freeland, G. Srajer, J. Stremper, G. Khaliullin, J. C. Cezar, T. Charlton, R. Dalgliesh, C. Bernhard, G. Cristiani, H.-U. Habermeier, and B. Keimer, *Nat. Phys.* **2**, 244 (2006).
 - [14] C. Schlueter, N. Yang, C. Mazzoli, C. Cantoni, A. Tebano, D. Di Castro, G. Balestrino, P. Orgiani, A. Galdi, J. Herrero-Martin, P. Gargiani, M. Valvidares, and C. Aruta, *Adv. Quantum Technol.* **3**, 2000016 (2020).
 - [15] C. Schlueter, C. Aruta, N. Yang, A. Tebano, D. Di Castro, G. Balestrino, and T. L. Lee, *Phys. Rev. Mat.* **3**, 094406 (2019).
 - [16] T. K. Nath, R. A. Rao, D. Lavric, C. B. Eom, L. Wu, and F. Tsui, *Appl. Phys. Lett.* **74**, 1615 (1999).
 - [17] A. Galdi, C. Sacco, P. Orgiani, F. Romeo, and L. Maritato, *J. Cryst. Growth* **459**, 56 (2017).
 - [18] S. Stemmer and A. J. Millis, *MRS Bull.* **38**, 1032 (2013).

- [19] Q.-R. Li, M. Major, M. B. Yazdi, W. Donner, V. H. Dao, B. Mercey, and U. Lüders, *Phys. Rev. B* **91**, 035420 (2015).
- [20] P. D. C. King, H. I. Wei, Y. F. Nie, M. Uchida, C. Adamo, S. Zhu, X. He, I. Božović, D. G. Schlom, and K. M. Shen, *Nat. Nanotechnol.* **9**, 443 (2014).
- [21] C. Sacco, A. Galdi, F. Romeo, N. Coppola, P. Orgiani, H. I. Wei, B. H. Goodge, L. F. Kourkoutis, K. Shen, D. G. Schlom, and L. Maritato, *J. Phys. D: Appl. Phys.* **52**, 135303 (2019).
- [22] T. S. Santos, B. J. Kirby, S. Kumar, S. J. May, J. A. Borchers, B. B. Maranville, J. Zarestky, S. G. E. teVelthuis, J. van den Brink, A. Bhattacharya, *Phys. Rev. Lett.* **107**, 167202 (2011).
- [23] C. Aruta, C. Adamo, A. Galdi, P. Orgiani, V. Bisogni, N. B. Brookes, J. C. Cezar, P. Thakur, C. A. Perroni, G. De Filippis *et al.*, *Phys. Rev. B* **80**, 140405(R) (2009).
- [24] S. J. Carreira, M. H. Aguirre, J. Briatico, and L. B. Steren, *RSC Adv.* **9**, 38604 (2019).
- [25] S. Koohfar, A. B. Georgescu, A. N. Penn, J. M. LeBeau, E. Arenholz, and D. P. Kumah, *npj Quantum Mater.* **4**, 25 (2019).
- [26] L. Maurel, N. Marcano, T. Prokscha, E. Langenberg, J. Blasco, R. Guzmán, A. Suter, C. Magén, L. Morellón, M. R. Ibarra, J. A. Pardo, and P. A. Algarabel, *Phys. Rev. B* **92**, 024419 (2015).
- [27] C. Aruta, G. Ghiringhelli, A. Tebano, N. G. Boggio, N. B. Brookes, P. G. Medaglia, and G. Balestrino, *Phys. Rev. B* **73**, 235121 (2006).
- [28] D. L. Windt, *Comput. Phys.* **12**, 360 (1998).
- [29] K. Persson, Materials Data on SrMnO₃ (SG:221) by Materials Project, The Materials Project. (2020); <https://doi.org/10.17188/1349743>
- [30] B. Li, R. V. Chopdekar, E. Arenholz, A. Mehta, and Y. Takamura, *Appl. Phys. Lett.* **105**, 202401 (2014).
- [31] A. Vailionis, H. Boschker, W. Siemons, E. P. Houwman, D. H. A. Blank, G. Rijnders, and G. Koster, *Phys. Rev. B* **83**, 064101 (2011).
- [32] O. Chmaissem, B. Dabrowski, S. Kolesnik, J. Mais, J. D. Jorgensen, and S. Short, *Phys. Rev. B* **67**, 094431 (2003).
- [33] B. H. Frazer, B. Gilbert, B. R. Sonderegger, and G. De Stasio, *Surf. Sci.* **537**, 161 (2003).
- [34] A. Ruosi, C. Raisch, A. Verna, R. Werner, B. A. Davidson, J. Fujii, R. Kleiner, and D. Koelle, *Phys. Rev. B* **90**, 125120 (2014).
- [35] C. Aruta, G. Ghiringhelli, V. Bisogni, L. Braicovich, N. B. Brookes, A. Tebano, and G. Balestrino, *Phys. Rev. B* **80**, 014431 (2009).
- [36] R. D. Cowan, *The Theory of Atomic Structure and Spectra* (University of California Press, Berkeley, 1981).
- [37] P. Carra, B. T. Thole, M. Altarelli, and X. Wang, *Phys. Rev. Lett.* **70**, 694 (1993).
- [38] W. L. O'Brien and B. P. Tonner, *Phys. Rev. B* **50**, 12672 (1994).
- [39] H. Zenia, G. A. Gehring, G. Banach, and W. M. Temmerman, *Phys. Rev. B* **71**, 024416 (2005).
- [40] A. Galdi, C. Aruta, P. Orgiani, C. Adamo, V. Bisogni, N. B. Brookes, G. Ghiringhelli, D. G. Schlom, P. Thakur, and L. Maritato, *Phys. Rev. B* **85**, 125129 (2012).
- [41] V. Skumryev, S. Stoyanov, Y. Zhang, G. Hadjipanayis, D. Givord, and J. Nogués, *Nature (London)* **423**, 850 (2003).
- [42] F. Li, C. Song, Y. Y. Wang, B. Cui, H. J. Mao, J. J. Peng, S. N. Li, G. Y. Wang, and F. Pan, *Sci. Rep.* **5**, 16187 (2015).
- [43] R. Søndénå, P. Ravindran, S. Stølen, T. Grande, and M. Hanfland, *Phys. Rev. B* **74**, 144102 (2006).
- [44] W. Wang, J. Zhang, X. Shen, X. Guan, Y. Yao, J. Li, C. Gu, J. Sun, Y. Zhu, J. Tao, and R. Yu, *Phys. Rev. B* **101**, 024406 (2020).